Simulating Waves in Flows by Runge–Kutta and Compact Difference Schemes

S.-T. Yu, K.-C. Hsieh, Y.-L. P. Tsai

Reprinted from

AIAA Journal

Volume 33, Number 3, Pages 421–429

AIAA

A publication of the
American Institute of Aeronautics and Astronautics, Inc.
370 L'Enfant Promenade, SW
Washington, DC 20024-2518

AIAA JOURNAL
Vol. 33, No. 3, March 1995

Simulating Waves in Flows by Runge–Kutta and Compact Difference Schemes

Sheng-Tao Yu,* Kwang-Chung Hsieh,† and Y.-L. Peter Tsai‡
NYMA Technology, Inc., Brook Park, Ohio 44142

The solution procedure of the unsteady Euler equations by various combinations of Runge–Kutta (RK) methods and compact difference (CD) schemes is investigated. Fourier analysis is performed on the fully discretized equation to assess the numerical accuracy and stability. The results clearly show a significant improvement of numerical characteristics by using the fourth-order CD scheme compared to the second-order one. Further increase of the order of the spatial differencing, however, results in little improvement. For time marching, the fourth-order RK scheme enlarges the time step for stable calculation as compared to a third-order one. Four numerical examples are included: acoustic waves in a converging nozzle, shocked sound waves in a straight tube, a single vortex in a uniform flow, and a vortex pairing. The fourth-order RK method combined with fourth- and sixth-order CD schemes shows crisp resolution of unsteady flow structures.

Nomenclature

A = acoustic admittance
a = cross-sectional area
c = speed of sound
c^* = speed of sound at a choked nozzle throat
$\boldsymbol{E}$ = inviscid flux
$\boldsymbol{E}_i$ = inviscid flux in i direction
F = CFL number
g = amplification factor
$\boldsymbol{H}$ = source term vector of the flow equations
k = boundary condition vector
k = nondimensionalized wave number
M = Mach number
P = amplitude of pressure wave
p = pressure
$\bar{p}$ = pressure of base flow
p' = pressure fluctuation of a wave
$\boldsymbol{Q}$ = flow variable vector
R = inhomogeneous term in the RK scheme
r = radial coordinate
t = time coordinate
U = amplitude of velocity wave
u = velocity in x direction
$\bar{u}$ = velocity of base flow in x direction
u' = velocity fluctuation in x direction
$\bar{v}$ = velocity of base flow in y direction
v' = velocity fluctuation in y direction
x = streamwise coordinate
Z = Fourier symbol of the discretized convective term
z = nondimensionalized distance
α = artificial dispersion
$\hat{\alpha}$ = nondimensional artificial dispersion
β = normalized frequency
γ = specific heat ratio
δ = spatial difference operator
η = coefficient of added artificial damping
θ = phase angle of the acoustic admittance
ξ = prescribed value of boundary condition
ρ = density
τ = nondimensionalized time

Received May 6, 1994; revision received Oct. 21, 1994; accepted for publication Oct. 27, 1994.

*Senior Research Engineer, Combustion and Icing Section, NASA Lewis Research Center. Member AIAA.
†Senior Scientist, Microgravity Section, NASA Lewis Research Center.
‡Senior Research Engineer, Computational Physics Section, NASA Lewis Research Center. Student Member AIAA.

I. Introduction

FOR unsteady flows, the phase velocities and harmonic content of numerical results are of concern. As a result of the discretization procedure, however, the simulated waves propagate in a dispersive and dissipative numerical medium. Consequently, the numerical characteristics of the scheme employed, such as the dispersive relation and the associated artificial damping, may greatly impact the numerical accuracy.

Recent development of time-accurate solutions of flowfields related to aeroacoustics has rekindled the use of high-order compact difference (CD) schemes. According to Colatz,[1] the CD scheme is Hermite's generalization of Taylor's series. As a contrast to the conventional central difference schemes, the CD methods use less grid nodes for high-order discretization. In the past, due to this unique advantage, many researchers used the CD schemes in solving various flow problems. Hirsh[2] employed a fourth-order CD to solve boundary layers and driven cavity flows. Agarwal[3] used the fourth-order CD to solve the Navier–Stokes equations for driven cavity flows. Harten and Tal-Ezer[4] studied the conservation property of the CD scheme for shock capturing. Philips and Rose[5] used various CD methods to solve the shock tube problem. Ciment and Leventhal[6] used the CD scheme for two-dimensional wave propagation.

More recently, Lele[7] applied the CD methods to simulate flowfield related to aeroacoustics. In his paper, CD schemes up to the 10th order were tabulated and Fourier analysis of a semidiscretized equation was performed. Since the time derivative was kept in an analytical form, Lele's analysis showed only the difference of CD schemes. Numerical characteristics of the Runge–Kutta (RK) time marching methods combined with CD schemes are still largely unclear. As a result, Lele solved the Navier–Stokes equations to simulate waves in flows and resorted to physical viscous terms for numerical stability. In addition, given a long list of CD schemes at high orders, it was unclear which one should be adopted for reasonable simulations.

In the present paper, we solve the quasi-one-dimensional and two-dimensional Euler equations by the RK methods for time marching and CD schemes for the spatial discretization. Fourier analysis is performed on the fully discretized equation to assess the numerical characteristics of various combinations of RK methods and CD schemes. Specifically, third- and fourth-order RK methods are considered for time marching. For spatial differencing, a conventional second-order central differencing (CD2), a fourth-order Pade's method (CD4), and a sixth-order CD scheme (CD6) are considered. This work is

intended to assess the overall performance of the RK-CD methods. As a result, the Courant-Friedrichs-Lewy (CFL) number limit, the numerical dispersion relation, and the required artificial damping for a stable and accurate solution are provided. The findings from the analysis are then supported by numerical examples.

In Sec. II, the numerical schemes of concern are presented in detail. Since we are interested in time-accurate flow solutions, the criteria for three- and four-step RK methods to be third- and fourth-order time accurate are briefly discussed. Section III illustrates Fourier analysis of the numerical schemes. The results of the analysis serve as a yard stick for calculating the four numerical examples presented in Sec. IV. The first case is a quasi-one-dimensional calculation of the acoustic admittance in a converging nozzle. The second case is a one-dimensional simulation of a shocked sound wave. The third and fourth cases involve two-dimensional vortices in a uniform flow. The calculated results are compared with available analytical solutions.

II. Numerical Method

The Euler equations in Cartesian coordinates can be cast into a vector form as

$$\frac{\partial \boldsymbol{Q}}{\partial t} + \frac{\partial \boldsymbol{E}_i}{\partial x_i} = \boldsymbol{H} \tag{1}$$

where $\boldsymbol{Q}$ is the unknown vector, $\boldsymbol{E}_i$ the inviscid flux in the x_i direction, and $\boldsymbol{H}$ the source term. Third- and fourth-order RK methods are applied as the time marching method, and second-, fourth-, and sixth-order CD schemes as the spatial discretization.

A. Runge–Kutta Method

An N-step RK method subdivides one time marching step into N steps on the interval $t^n \le t \le t^{n+1}$, and the object function is integrated explicitly at each step, i.e.,

$$\begin{aligned} Q^1 &= Q^n + \Delta t\left(\alpha_{11} R^n\right) \\ Q^2 &= Q^n + \Delta t\left(\alpha_{21} R^n + \alpha_{22} R^1\right) \\ Q^3 &= Q^n + \Delta t\left(\alpha_{31} R^n + \alpha_{32} R^1 + \alpha_{33} R^2\right) \\ &\vdots \\ Q^{n+1} &= Q^n + \Delta t\left(\alpha_{N1} R^n + \alpha_{N2} R^1 + \cdots + \alpha_{NN} R^{N-1}\right) \end{aligned} \tag{2}$$

where the superscripts n, 1, 2, ..., and $n+1$ denote the steps on the interval, i.e., $t^n \le t_1 \le t_2 \le \cdots \le t_N \le t^{n+1}$; α_{ij} is the weighting coefficient for step i and term j; Q is the object function to be integrated; and R^n, R^1, R^2, ..., R^{N-1} is the evaluation of the spatial derivatives and the source term based on Q^n, Q^1, Q^2, ..., Q^{N-1}. For convenience, we denote R as the inhomogeneous term. As shown in Eq. (2), the increment of the object function at each intermediate step is a weighted average of the inhomogeneous terms evaluated at the previous steps. As a result, there are $N(1+N)/2$ weighting coefficients to be determined.

For nonlinear equations, to retain the prescribed order of accuracy, the RK scheme can be fitted into a Taylor's series to deduce a constraint of the weighting coefficients. The constraint is in the form of a set of algebraic equations in terms of weighting coefficients. In general, there are less equations than unknowns. Consequently, various RK methods were developed by taking the liberty of choosing the coefficients within the constraint.

For a three-step RK method, six coefficients are constrained by four equations which are tabulated in Ref. 8. Here, we use Wray's three-step method.[9]

$$\begin{aligned} Q^1 &= Q^n + \Delta t\left(\tfrac{8}{15} R^n\right) \\ Q^2 &= Q^n + \Delta t\left(\tfrac{1}{4} R^n + \tfrac{5}{12} R^1\right) \\ Q^{n+1} &= Q^n + \Delta t\left(\tfrac{1}{4} R^n + \tfrac{3}{4} R^2\right) \end{aligned} \tag{3}$$

It can be shown that Wray's weighting coefficients satisfy the constraint in Ref. 8 for the third-order accuracy.

A similar procedure can be applied to a four-step RK method for the fourth-order time accuracy. There are seven equations for 10 coefficients. Here, we use Kutta's four-step RK method[8] which was first employed by Jameson et al.[10] for solving flow equations. The algorithm can be expressed as

$$\begin{aligned} Q^1 &= Q^n + \frac{\Delta t}{2} R^n \\ Q^2 &= Q^n + \frac{\Delta t}{2} R^1 \\ Q^3 &= Q^n + \Delta t R^2 \\ Q^{n+1} &= Q^n + \frac{\Delta t}{6}\left(R^n + 2R^1 + 2R^2 + R^3\right) \end{aligned} \tag{4}$$

One can show that Kutta's coefficients satisfy the fourth-order constraint.

There is another more popular and less complex four-step RK scheme proposed by Jameson and Baker[11] for flow calculations. As a contrast to the present method in Eq. (4), the calculation of the final step of this popular scheme[11] involves only one inhomogeneous term evaluated at a previous step instead of all four steps as that in Eq. (4). Therefore, the scheme is more efficient. However, this scheme was designed to hasten the numerical convergence for steady-state solutions, and the coefficients do not satisfy the fourth-order constraint.

B. Compact Difference Schemes

According to Colatz,[1] the CD4 and CD6 schemes were obtained by using three and five grid nodes in the computational domain. The gain in the accuracy is not based on the use of more points, as in the conventional approach, but on implicitly solving the derivatives at the grid nodes, i.e.,

$$u'_{i-1} + 4u'_i + u'_{i+1} = (3/\Delta x)(u_{i+1} - u_{i-1}) + \mathcal{O}(\Delta x^4) \tag{5}$$

$$u'_{i-1} + 3u'_i + u'_{i+1} = (1/12\Delta x)(u_{i+2} - 28u_{i+1} - 28u_{i-1} - u_{i-2}) + \mathcal{O}(\Delta x^6) \tag{6}$$

where the superscript prime represents the spatial derivatives. The application of these CD schemes involves the inversion of a scalar tridiagonal matrix that incurs little penalty in terms of CPU time.

When the CD4 is used in the interior nodes, a third-order biased implicit scheme proposed by Adam[12] is employed for grid nodes at computational boundaries

$$\begin{aligned} 2u'_1 + 4u'_2 &= (1/\Delta x)(-5u_1 + 4u_2 + u_3) + \mathcal{O}(\Delta x^3) \\ 2u'_{\max} + 4u'_{\max-1} &= (1/\Delta x)(5u_{\max} - 4u_{\max-1} - u_{\max-2}) + \mathcal{O}(\Delta x^3) \end{aligned} \tag{7}$$

When CD6 is used in the interior nodes, we use CD4 at locations one grid node away from the boundary and the third-order biased scheme is used at the boundary. In addition, as will be shown in Sec. IV, a method-of-characteristics-(MOC-) type nonreflecting boundary condition is incorporated with the third-order biased difference at the computational boundary. This treatment allow numerical waves to propagate out of the computational domain.

III. Fourier Analysis

The background for Fourier analysis on discretized equations can be found in Ref. 13. Since the equations are discretized by a finite difference scheme, the harmonic content is limited to the number of grid nodes used in the computational domain. For a computational domain L decomposed into K grid nodes ($L = K\Delta x$), the discrete solution u_j^n at a location (j) and time (n) is a linear combination of K wave modes. The discrete Fourier expansion is performed on the discretized equation to deduce the amplification factor $g(k)$

$$g(k) = \frac{\hat{u}^{n+1}(k)}{\hat{u}^n(k)} \tag{8}$$

where $\hat{u}$ is the Fourier coefficient of u. Since the analysis is local for an infinite and periodic domain, the result of Fourier analysis is presented on the interval $[0, \pi]$.

We employ a scalar, advective equation as the model equation,

$$\frac{\partial u}{\partial t} + \lambda \frac{\partial u}{\partial x} = 0 \tag{9}$$

where the phase velocity λ is equivalent to the eigenvalues of the Jacobian matrix in the one-dimensional Euler Equations, namely, $u - c$, $u + c$, and u, where u is the velocity and c is the speed of sound. Following Jameson and Baker,[10] the amplification factors for the three- and four-step Runge–Kutta methods are

$$g = 1 + Z + \tfrac{1}{2}Z^2 + \tfrac{1}{6}Z^3 \tag{10}$$

$$g = 1 + Z + \tfrac{1}{2}Z^2 + \tfrac{1}{6}Z^3 + \tfrac{1}{24}Z^4 \tag{11}$$

The variable Z is the Fourier symbol of the discretized convective term. To obtain Z, we formulate the CD4 method in an operator form which allows us to express $(\partial u/\partial x)_i$ explicitly as

$$\left(\frac{\partial u}{\partial x}\right)_i = \left(1 + \frac{\delta^2}{6}\right)^{-1} \left(\frac{u_{i+1} - u_{i-1}}{2\Delta x}\right) + \mathcal{O}(\Delta x^4) \tag{12}$$

where

$$\delta^2 u_i = u_{i+1} - 2u_i + u_{i-1} \tag{13}$$

Substitute Eq. (12) into the discretized model equation, Eq. (9), and we obtain

$$Z^{(4)} = -\frac{6F \sin(\hat{k})i}{4 + 2\cos(\hat{k})} \tag{14}$$

where the superscript (4) represents the CD4 method; $F = \lambda \Delta t/\Delta x$; and $\hat{k}$ is the normalized wave number $\hat{k} = 2\pi k/K$.

Similarly, the CD6 scheme is represented in operator form as

$$\frac{\partial u}{\partial x} = \left(1 + \frac{\delta^2}{5}\right)^{-1} \frac{1}{60\Delta x}(u_{i+2} + 28u_{i+1} - 28u_{i-1} - u_{i-2}) + \mathcal{O}(\Delta x^6) \tag{15}$$

and we obtain

$$Z^{(6)} = -\frac{F[4\sin(\hat{k})\cos(\hat{k}) + 56\sin(\hat{k})]i}{12[2\cos(\hat{k}) + 3]} \tag{16}$$

Substituting $Z^{(4)}$ and $Z^{(6)}$ into the amplification factors Eqs. (10) and (11), we obtain $g(\hat{k})$ for various combinations of the RK methods and CD schemes. In general, $g(\hat{k})$ is a complex number and can be expressed as

$$g(\hat{k}) = |g(\hat{k})|e^{i\alpha(\hat{k})} \tag{17}$$

To present the result of Fourier analysis, we make the following interpretations.

1) Numerical dissipation: The magnitude of the amplification factor is the artificial dissipation. When $|g| \geq 1$, the scheme is unstable. For the calculations of unsteady flows, we want $|g|$ to be less than unity but as large as possible to ensure numerical stability with minimum artificial dissipation. In the following section, we plot $|g|$ against $\hat{k}$ to illustrate the artificial dissipation.

2) Numerical dispersion. In Eq. (17), $\alpha(\hat{k})$ represents the artificial dispersion. We plot $\hat{\alpha} = \alpha/F$ against $\hat{k}$ to show phase velocities. Notice that the model equation is dispersionless, and the phase velocity is a constant. After being normalized by the CFL number, the exact solution is a straight line with 45-deg angle on the plot of $\hat{\alpha}$ against $\hat{k}$.

Figure 1 shows the results of the Fourier analysis of the RK3 method combined with CD2, CD4, and CD6 schemes. The figures show the dissipative as well as dispersive effects at CFL numbers

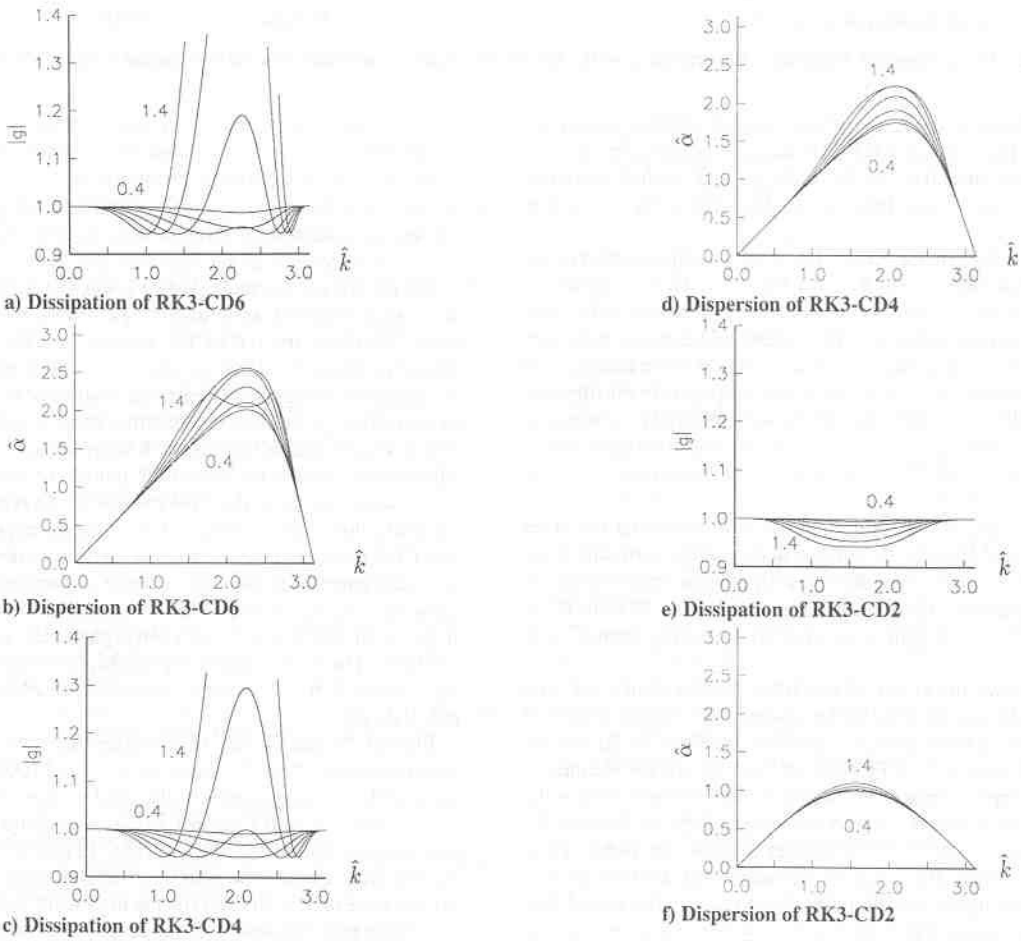

Fig. 1 Dissipation and dispersion characteristics of the RK3 time stepping combined with various spatial discretization schemes.

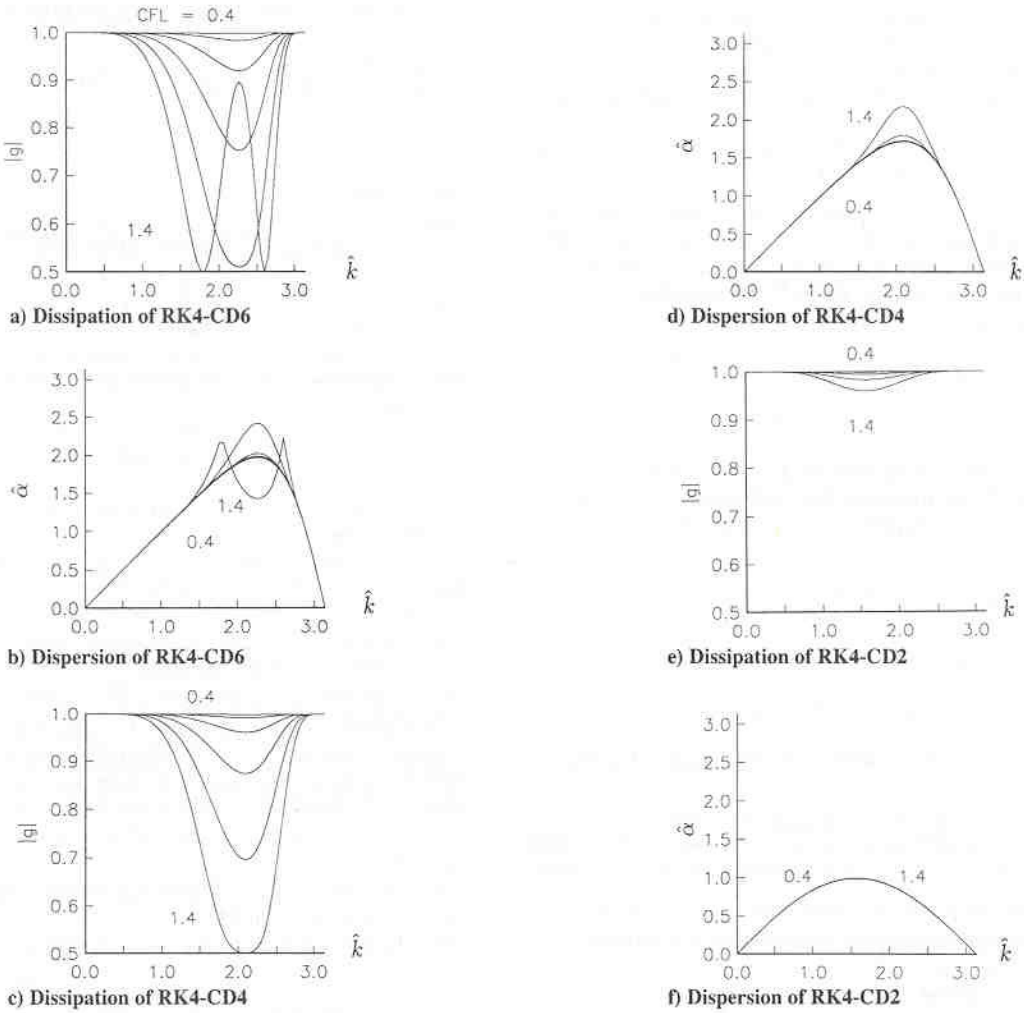

Fig. 2 Dissipation and dispersion characteristics of the RK4 time stepping combined with various spatial discretization schemes.

from 0.4 to 1.4 with an increment of 0.2 between neighboring curves. According to Fig. 1a, the RK3-CD6 scheme is unstable for CFL numbers greater than 0.8. As the order of CD method increases (compare Figs. 1a, 1c, and 1e), the CFL limit for stable calculation decreases.

According to Fig. 1b, the RK3-CD6 scheme retains correct phase velocity wave numbers up to $\pi/2$ at CFL = 0.4. That is, numerical waves resolved by four and more than four grid nodes suffer little dispersive error. Increasing the CFL number makes phase velocities deviate from the 45-deg straight line at a smaller wave number. For high wave numbers, i.e., $\hat{k} \approx \pi$, the waves propagate in the opposite direction than they should. These waves were referred to as parasitic waves. When using higher order CD schemes, these parasitic waves do not go away for all CFL numbers and the combinations of the schemes.

Comparing Figs. 1b, 1d, and 1f shows that increasing the order of the CD method reduces the numerical dispersion at middle wave numbers ($1 \leq \hat{k} \leq 2$). Specifically, a significant improvement is achieved by changing the spatial differencing from CD2 to CD4, whereas only a limited gain is obtained by switching from CD4 to CD6.

Figure 2 shows the result of the RK4 method combined with various CD schemes. Similar to the case of RK3, higher order CD schemes introduce more artificial damping (see Figs. 2a, 2c, and 2e) and, therefore, reduce the CFL number limit for stable calculation. Again, the dispersive error at middle wave numbers decreases as the order of the spatial differencing increases (see Figs. 2b, 2d, and 2f).

In Figs. 1 and 2, the result of Fourier analysis are presented in a continuous fashion. However, the numerical calculations are dictated by discrete points distributed in these curves. The useful data points in the wave number region of $\pi/2 \leq \hat{k} \leq \pi$ are very sparse. For example, $\hat{k} = \pi$ represents waves resolved by two grid nodes, $\hat{k} = 2\pi/3$ represents three-node waves, and $\hat{k} = \pi/2$ is four-nodes waves. Numerically, the two-node waves represent even-odd decoupling, and they are parasitic. Similarly, a wave delineated by three grid nodes is not very meaningful. Therefore, we want to concentrate on the numerical resolution in the wave number region $0 \leq \hat{k} \leq \pi/2$, i.e., for wavelengths larger than four grid nodes.

For the RK4-CD6 method at CFL = 0.8 (see Fig. 2b) the solution with wave numbers up to about $\pi/2$ suffers from little dispersive error. Similarly, the RK4-CD4 scheme (see Fig. 2d) suffers little dispersive error for wave number up to about $\pi/2$. Therefore, the advantage of using the CD6 scheme instead of CD4 in terms of dispersive errors is limited. On the other hand, comparison of Figs. 2a and 2c clearly shows that the CD6 scheme contains a little more artificial dissipation at the same CFL numbers for four- and five-node waves as compared to the CD4 method. For a typical calculation of unsteady flows, the minimum wave length resolved by both CD4 and CD6 methods is about four to six grid nodes. And the numerical performance of the CD6 scheme is comparable to that of the CD4 scheme. According to the foregoing discussion, there is little, if any at all, advantage to use even higher order compact difference schemes. The CD4 method is probably the most efficient and stable scheme with a reasonable numerical resolution for large-scale calculations.

Figures 1c and 2c can be compared to show the difference of the dissipation effects between the RK3 and RK4 methods. For the same CFL and wave numbers, the RK4 method introduces more artificial damping, and a larger CFL number could be used for stable calculations. On the other hand, Figs. 1d and 2d show that increasing the order of the time marching scheme from RK3 to RK4 does not improve the dispersive effect at high wave numbers. The dispersive effect is dominated by the spatial discretization. Therefore, one should always use the RK4 method instead of the RK3 method.

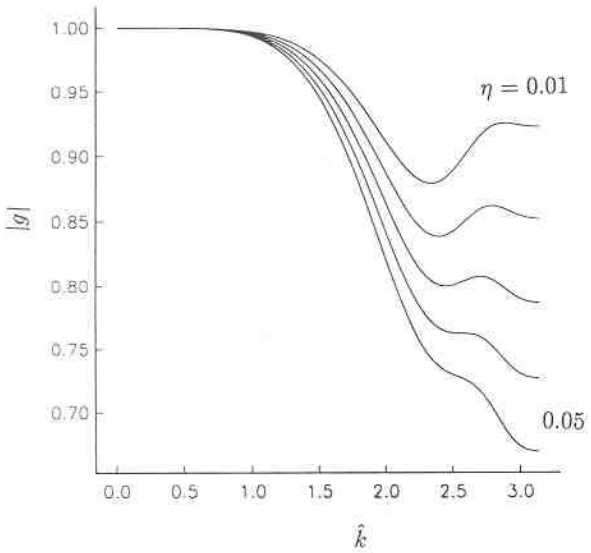

a)

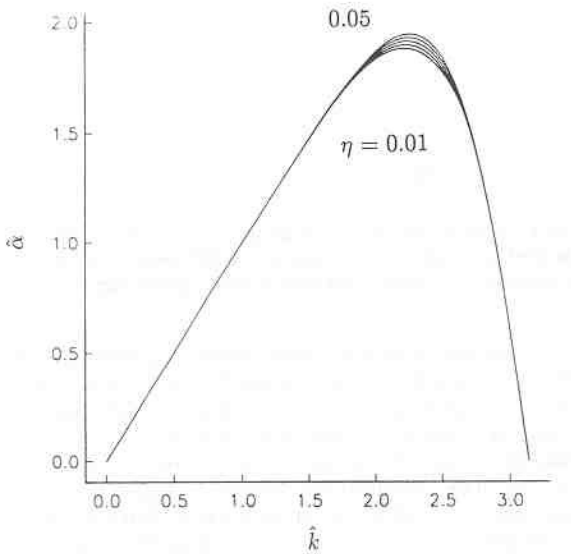

b)

Fig. 3 Dissipation and dispersion characteristics of the RK4-CD6 method with various amounts of the sixth-order numerical damping.

As shown in Figs. 1 and 2, CD schemes have no dissipative effects at high wave numbers. Nevertheless, dispersive error causes these waves to propagate in the erroneous direction, and they will eventually destroy the solution. It is, therefore, appropriate to impose a small amount of artificial damping to filter out these waves and at the same time keep the resolution at low wave modes intact. Figure 3 shows the dissipation and dispersion effects of the RK4-CD6 method at CFL = 0.8 with various amounts of a sixth-order artificial damping (AD), defined as

$$\mathrm{AD} = (\eta/8)[u_{i+3} + u_{i-3} - 6(u_{i+2} + u_{i-2}) + 15(u_{i+3} + u_{i-3}) - 20u_i] \tag{18}$$

The range of η is from 0.01 to 0.05 with an increment of 0.01 between the neighboring curves. Comparison between Fig. 3 and Figs. 2a and 2b shows that no additional damping at low wave numbers is introduced into the system by the imposed artificial viscosity for $\eta \leq 0.03$, whereas the undesirable high wave number waves are dissipated.

IV. Numerical Examples

A. Acoustic Admittance of a Converging Nozzle

The first case is a forced oscillatory quasi-one-dimensional flow in a converging nozzle. The governing equations are

$$\frac{\partial \boldsymbol{Q}}{\partial t} + \frac{\partial \boldsymbol{E}}{\partial x} = \boldsymbol{H} \tag{19}$$

where

$$\boldsymbol{Q} = \begin{pmatrix} \rho \\ \rho u \\ e \end{pmatrix} a, \qquad \boldsymbol{E} = \begin{pmatrix} \rho \\ \rho u^2 + p \\ (e+p)u \end{pmatrix} a, \qquad \boldsymbol{H} \begin{pmatrix} 0 \\ p\dfrac{\mathrm{d}a}{\mathrm{d}x} \\ 0 \end{pmatrix} \tag{20}$$

where ρ is density, p pressure, and e total energy defined as $e = \rho(C_v T + \frac{1}{2}u^2)$ where C_v is the constant volume specific heat. The variable a is the cross-sectional area and is prescribed as a function of x. The theoretical solution of the acoustic admittance of a choked nozzle was provided by Tsien[14] under the assumption that the velocity of the base flow is a linear function of axial location. The nozzle shape can be inversely derived according to Tsien's assumption, and we have

$$a = \frac{1}{M}\left(\frac{2}{\gamma+1} + \frac{\gamma-1}{\gamma+1}M^2\right)^{\frac{\gamma+1}{2(\gamma-1)}} \tag{21}$$

where γ is the specific heat ratio and M is the Mach number which can be expressed as

$$M = \frac{x}{x^*}\sqrt{\frac{\gamma+1}{2} - \frac{\gamma-1}{2}\left(\frac{x}{x^*}\right)^2} \tag{22}$$

The superscript asterisk denotes the property at the nozzle throat. According to Tsien's derivation, the linearized quasi-one-dimensional equations can be manipulated to the following form under the isentropic condition:

$$z(1-z)\frac{\mathrm{d}^2 P}{\mathrm{d}z^2} - 2\left(1 + \frac{i\beta}{1+\gamma}\right)z\frac{\mathrm{d}P}{\mathrm{d}z} - i\beta\frac{(2+i\beta)}{2(\gamma+1)}P = 0 \tag{23}$$

$$(\gamma+1)(1-z)\frac{\mathrm{d}P}{\mathrm{d}z} - (\gamma - 1 + i\beta)P + (2+i\beta)U = 0 \tag{24}$$

where

$$(p'/\gamma\bar{p}) = P(z)e^{i\beta\tau}, \qquad (u'/\bar{u}) = U(z)^{i\beta\tau} \tag{25}$$

and $\bar{u}$ and $\bar{p}$ are the velocity and pressure of the base flow, β is the normalized frequency which is defined as $\beta = \omega(1-z)/(\bar{c}^* - \bar{u})$, and τ is the nondimensionalized time which is defined as $\tau = \bar{c}^* t/x^*$. The independent variable z can be expressed in different forms due to the linearity between the base flow velocity $\bar{u}$ and axial location x, and we have

$$z = \frac{x}{x^*} = \frac{\bar{u}}{c^*} = \frac{(\gamma+1)M^2}{2 + (\gamma-1)M^2} \tag{26}$$

With Eq. (26), it is clear that P and U are functions of the Mach number M. Equation (23) is a hypergeometric equation[15] that can be solved by a power series expansion. $U(z)$ can be easily solved with $P(z)$ known as shown in Eq. (24). Finally, the acoustic admittance function defined as $A(z) = U(z)/P(z)$ can be obtained as a function of the Mach number.

In what follows, the procedure of the CFD calculation for comparison with Tsien's solution is illustrated. First, the base flowfield is obtained by solving the quasi-one-dimensional equations, Eqs. (19) and (20), using the RK4-CD2 method with the nozzle area ratio prescribed by Eqs. (21) and (22). The results are checked by the classical area Mach number relation[16] and the solution is accurate up to five decimal digits. The perturbation at the inlet is obtained by specifying sinusoidal pressure fluctuations in terms of magnitude and frequency. With the prescribed pressure and isentropic correlation, the temperature fluctuation is also determined. Numerically, these boundary conditions are enforced by defining a vector $k = k(\boldsymbol{Q})$ at the upstream boundary, such as

$$k = \begin{pmatrix} p \\ T \\ 0 \end{pmatrix} = \begin{pmatrix} \xi_1 \\ \xi_2 \\ 0 \end{pmatrix} \tag{27}$$

Table 1 Errors of the acoustic admittance calculation

Numerical schemes	Error of $\|A\|$	Error of θ
RK4-CD6	0.45%	3.6%
RK4-CD4	0.52%	3.3%
RK4-CD2	1.65%	4.1%

where ξ_1 and ξ_2 are the specified values of p and T. To proceed, Eq. (27) is linearized to become a function of ΔQ, such as

$$k^{n+1} = k^n + \frac{\partial k}{\partial Q}\Delta Q \tag{28}$$

where k^{n+1} is equal to the specified pressure and temperature at the time step $n+1$ and $\partial k/\partial Q$ is a 3×3 matrix. To close the system, the null entry in the vector k may be filled by the out-running characteristic relation deduced from the flow equations. Numerically, the similarity transformation is applied to the discretized flow equations [see Eq. (2)], and we get

$$LM^{-1}(Q^i - Q^n) = LM^{-1}\Delta t \sum_{k=1}^{i} \alpha_{ik} R^{k-1} \tag{29}$$

where $i = 1, \ldots, N$ represents the N-step RK method. Here, M^{-1}, is the eigenvector matrix of Jacobian matrix $A = \partial E/\partial Q$, and L is a selection matrix with zeros and ones on the diagonal in such a fashion that the proper out-running characteristics are selected. By combining the imposed conditions, Eq. (28), with the out-running characteristic relations, Eq. (29), we form the complete equation at the boundary point as

$$\left(LM^{-1} + \frac{\partial k}{\partial Q}\right)(Q^i - Q^n) = LM^{-1}\Delta t \sum_{k=1}^{i} \alpha_{ik} R^{k-1} + k^{n+1} - k^n \tag{30}$$

For the supersonic out-flow condition, Eq. (29) is used with the selection matrix L equal to an identity matrix. The out-running characteristic equations are solved with one-sided difference as shown in Eq. (7). In other words, the characteristic boundary conditions are always discretized by an upwinding scheme which is physically sound, and the numerical stability is enhanced. These boundary conditions are applied at each intermediate step of the Runge–Kutta method.

The acoustic admittance is a complex number and can be written as $A = |A|e^{i\theta}$. In the present paper, a small pressure perturbation of 1.1% ($p' = 0.011\bar{p}$) is imposed at the nozzle inlet. The length of the converging part of the nozzle is $0.9L^*$ and the inlet Mach number is about 0.09. The frequency of the perturbation is set at $\beta = 6$, which corresponds to about 2000 Hz.

Figure 4 shows the comparisons between the CFD results of the RK4-CD6 method and the theoretical solution of the acoustic admittance in terms of the magnitude $|A|$ and the phase angle θ in a converging nozzle. Both the magnitude and the phase angle of the acoustic admittance decrease as the flow speeds up. As shown in the figure, perfect agreement is obtained for the comparison of $|A|$, whereas the predicted phase angle is slightly off due to the resolution of the numerical grid for the phase angle. In this case, the harmonic content of the solution is limited to one frequency with a wave length comparable to the computational domain which is resolved by 61 grid nodes. Therefore, all numerical schemes of concern provide accurate solutions. The numerical errors of $|A|$ and θ are tabulated in Table 1. There is a slight advantage in using the higher order schemes for the prediction of $|A|$; however, no obvious advantage of using the higher order scheme for the phase angle calculation is observed.

B. Shocked Sound Waves

The second case is the propagation of shocked sound waves in a tube with a periodic boundary condition. The governing equations are the same as in the first case, namely, Eqs. (19) and (20), with cross-sectional area a equal to a constant. This case is interesting

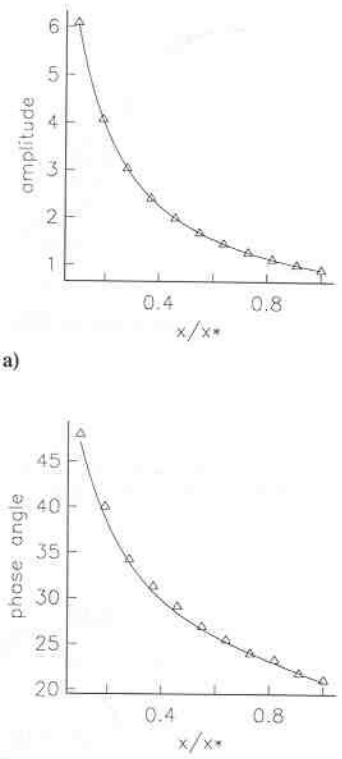

Fig. 4 Acoustic admittance calculation using the RK4-CD6 method for the inlet perturbation as $\beta = 6, p'/\bar{p} = 0.011$; solid line Tsien's theorem, triangles CFD results: a) magnitude and b) phase angle.

for its complex harmonic content compared to the first case. In addition, the capability of the high-order compact difference schemes for shock capturing can also be studied. At time equal to zero, a sinusoidal pressure distribution is given. Because of the periodic boundary condition, only one cycle resolved by 61 grid nodes is imposed in the computational domain. According to the isentropic condition, the distributions of temperature, density, and speed of sound are also determined. The velocity profile is determined by the simple wave correlation,[17] such that

$$u(x) = \int_{\bar{p}}^{p(x)} \frac{\mathrm{d}p}{\rho(x)c(x)} = \frac{2\gamma}{\gamma - 1}\sqrt{\frac{\bar{p}^{\frac{1}{\gamma}}}{\gamma\bar{p}}}\left[p(x)^{\frac{\gamma-1}{2\gamma}} - \bar{p}^{\frac{\gamma-1}{2\gamma}}\right] \tag{31}$$

where the average flow properties are denoted by a bar. With the simple wave correlation, the wave forms of all flow properties are in phase, and the initial condition of the present CFD computation matches the theoretical analysis provided by Morse and Ingard.[18] It is interesting to note that the simple wave correlation is an extension of a linear, plane, acoustic wave. For a variation of pressure less than 5%, the plane wave relations could be adopted, such that

$$T(x) = \bar{T}\left(1 + \frac{\gamma - 1}{\gamma}\frac{p'(x)}{\bar{p}}\right)$$
$$\rho(x) = \bar{p}\left(1 + \frac{p'(x)}{\gamma\bar{p}}\right) \tag{32}$$
$$u(x) = c(x)\frac{p'(x)}{\gamma\bar{p}}$$

where $p'(x)$ is the prescribed pressure fluctuation. As shown in Eqs. (31) and (32), the wave speeds $u+c$, $u-c$, and u vary as a result of the flow property distribution. The distortion of the wave form is a cumulative effect resulting from the wave speed distribution. For

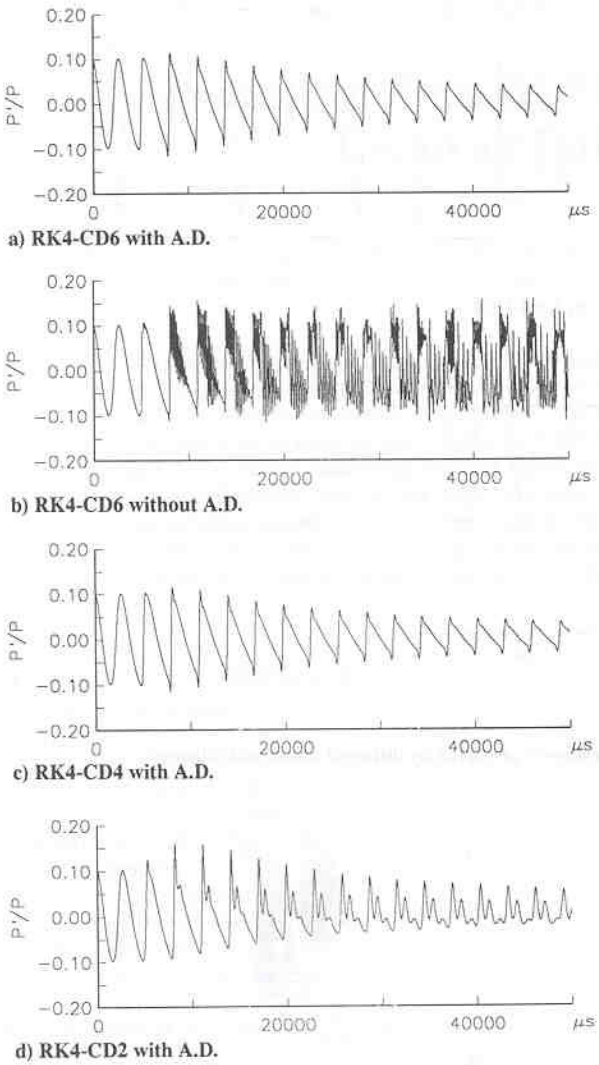

a) RK4-CD6 with A.D.

b) RK4-CD6 without A.D.

c) RK4-CD4 with A.D.

d) RK4-CD2 with A.D.

Fig. 5 Time history of the pressure fluctuations of the *N*-wave calculation at one end of the periodic domain by various numerical schemes.

simple waves, i.e., all flow properties are in phase, the wave crest will quickly overtake the trough and form a shock.

Figure 5 shows the time history of the pressure fluctuation at one end of the computational domain for various finite difference schemes. According to Morse and Ingard, the first shock appears after about two cycles for the case of a 10% pressure perturbation ($p'/\bar{p} = 0.1$) (Ref. 18). All schemes of concern predict the wave steepening rate correctly. After the wave is shocked, the flow evolution is no longer isentropic, and the kinetic energy is gradually converted to thermal energy due to the existence of the shock wave. As a result, the strength of the shock wave diminishes as time passes.

The shock front is a combination of many wave modes traveling at the same speed. The dispersion error introduced by the finite difference schemes will cause the high wave number waves to travel with erroneous speeds. As shown in Fig. 5, the methods of RK4-CD6 and RK4-CD4 with a small amount of the sixth-order artificial damping ($\eta = 0.02$) crisply resolve the shock except for the overshoots. These overshoots are caused by Gibbs phenomenon and can be fixed only by TVD-type shock-capturing schemes. Almost no difference can be observed between the results of the CD4 and CD6 methods. On the other hand, the method of RK4-CD6 without background filtering shows that significant high wave number waves lag behind the shock front because the compact difference scheme introduces no dissipative but high dispersive effects on the highest wave number waves. As shown in the figure, these oscillations eventually contaminate the whole solution. For the conventional RK4-CD2 method, results show significant oscillations of moderate wave numbers behind the shock front because of dispersion errors.

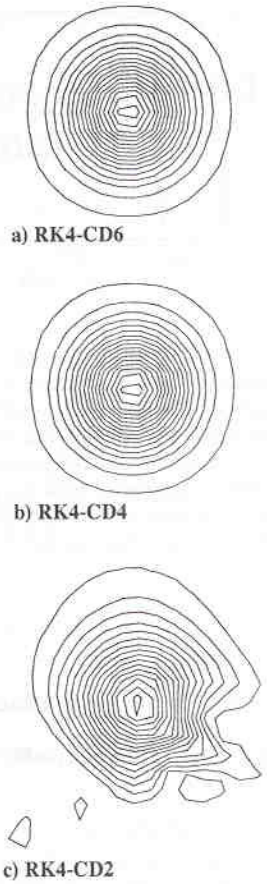

a) RK4-CD6

b) RK4-CD4

c) RK4-CD2

Fig. 6 Vorticity contours of the vortex after traveling about 60 core radii predicted by various numerical schemes.

C. Vortex Propagation in a Uniform Flow

A vortex translating in a uniform flow is chosen as a two-dimensional numerical example. The initial condition of the vortex is formulated analytically similar to that of Liu et al.[19] The vortex can be characterized by the circulation Γ and the core radius a. The azimuthal velocity u_θ at a distance r from the vortex center is given as,

$$u_\theta = \frac{\Gamma}{2\pi}\frac{r}{r^2 + a^2} \tag{33}$$

The flow near the vortex center is a rigid-body rotation ($u_\theta \propto r$). The flow far outside the core is irrotational ($u_\theta \propto 1/r$) with u_θ decreasing as r increases. Equation (33) is a continuous function to connect the two extremes. With the prescribed velocity field, the pressure and density distributions of the vortex can be determined by the momentum and the energy equations,

$$\frac{\partial p}{\partial r} = \rho\frac{u_\theta^2}{r} \tag{34}$$

$$\frac{\gamma}{\gamma - 1}\frac{p}{\rho} + \frac{u_\theta^2}{2} = h_0 \tag{35}$$

where h_0 is the total enthalpy and is set to be a constant such that $h_0 = \gamma\bar{p}/(\gamma - 1)\bar{p}$ with the freestream condition denoted by a bar. To proceed, substitute Eqs. (33) and (35) into Eq. (34) and integrate the equation over r. As a result, the pressure distribution is obtained. Consequently, the density distribution and the whole flowfield is determined. The solutions of this stationary vortex can be superimposed to any uniform flow with arbitrary speed. Physically, this process may be interpreted as a stationary vortex being observed from a moving coordinate system with constant velocity. Thus, the vortex in a uniform flow can be constructed as

$$u = \bar{u} + u', \qquad v = \bar{v} + v' \tag{36}$$

where the velocities of the background flow are denoted by a bar

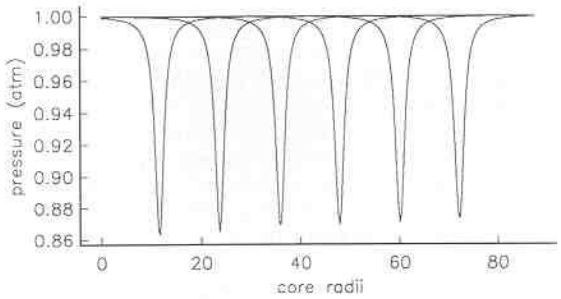

a) RK4-CD6

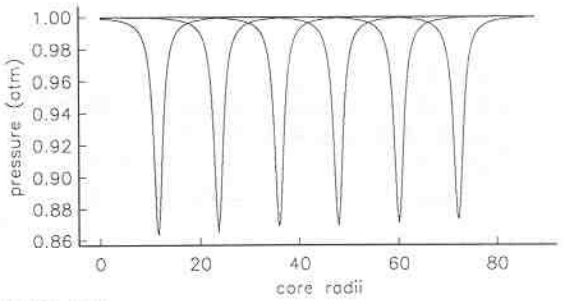

b) RK4-CD4

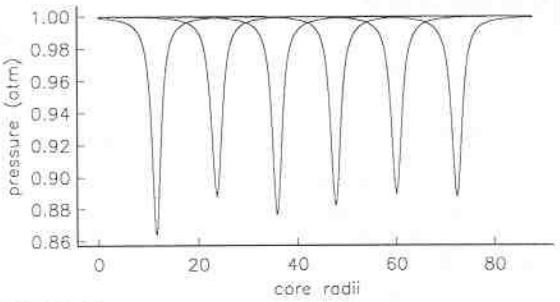

c) RK4-CD2

Fig. 7 Vortex pressure profiles at the centerline at various instances predicted by different numerical schemes.

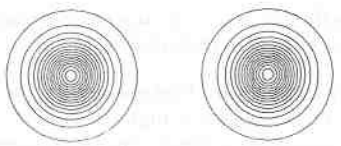

a)

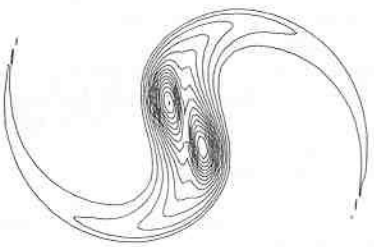

d)

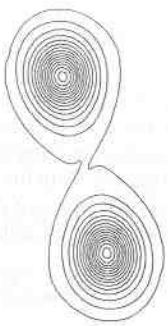

b)

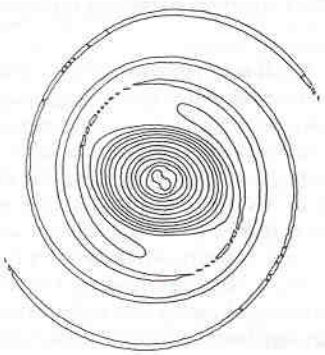

e)

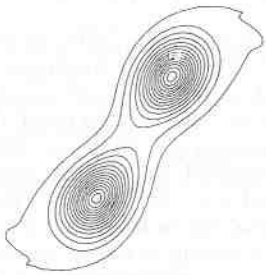

c)

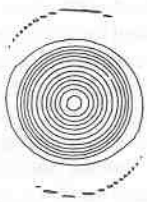

f)

Fig. 8 Vorticity contours of the vortex pairing.

and the superscript prime denotes the vortex velocities specified by Eq. (33). The pressure and density distribution of the moving vortex is the same as that of the stationary vortex and may be obtained from the solutions of Eqs. (34) and (35).

The boundary condition of the present case is an extension of the MOC-type treatment discussed in case 1. Essentially, only one-dimensional characteristics normal to the computational boundary are considered. For the imposed inflow condition, Giles's formulation[20] is employed.

The prescribed vortex flowfield contains a broadband of frequencies due to the distribution of the azimuthal velocity. Theoretically, all wave modes travel at the same speed to ensure the integrity of the vortex structure. For numerical methods with dispersive error, the shape of the vortex could deform, even break up in the later stage of the time marching procedure. In addition, the dissipation effect of finite difference schemes can be evaluated by the conservation of the sharp pressure dip at the center of the vortex.

In the present calculations, the Mach number of the background flow is 0.4. The grid size is 301×91 in the streamwise and transverse directions. The numerical mesh is uniform in the axial direction and stretched in the transverse direction near the outside boundary. The CFL number calculated based on the background flow is about 0.7 for all calculations. A small amount of background filtering, i.e., $\eta = 0.02$ in Eq. (18), is applied for all calculations. The core radius a is about 1 cm and is resolved by about 4 grid nodes.

Figure 6 shows the vorticity contours after the eddy propagates about 60 core radii downstream as simulated by various numerical schemes. Clearly, the structure of the eddy is retained by the compact difference schemes (CD4 and CD6). In contrast, the eddy predicted by the CD2 method is shattered due to the excessive dispersive error.

Figure 7 shows pressure distributions of the eddy at various instances. The x axis is the streamwise locations nondimensionalized by the core radius of the vortex, and the y axis is the pressure. For both CD4 and CD6 methods, the pressure at the vortex center increases about 1% through the process.

In comparison, the result of the CD2 scheme shows pressure increase about 3%. In addition, the pressure fluctuation shown in Fig. 7c is due to the deviation of the vortex path predicted by the CD2 method. Therefore, the dispersion error of the CD2 scheme is more severe than the dissipation error.

D. Vortex Pairing

The calculation of the single vortex is extended to a vortex pairing. The vortex pairing is the controlling mechanism for the growth of a mixing layer, and it occurs when the distance between two vortices is less than a threshold value. Although not shown, similar to the single eddy case, the results of the CD4 and CD6 are almost identical. In the present paper, the result of the RK4-CD6 method is presented.

The initial condition is specified by two identical vortices placed 5 core radii apart in a quiescent gas. The core radius is 1 cm, and the circulation is 15 m^2/s. At the center of each vortex, there is a pressure deficit about 15% compared to the ambient gas. The grid size is 201×201. The mesh is uniform at the center of the computational domain and slightly stretched near boundary. Figure 8 shows the contours of the vorticity magnitude at various stages of the vortex interaction. The whole sequence is about one-and-one-half revolutions.

V. Concluding Remarks

The quasi-one-dimensional and two-dimensional Euler solvers using various combinations of RK methods and CD schemes were analyzed for simulating unsteady flows. The accuracy of the employed schemes is assessed by Fourier analysis on the fully discretized equation. The numerical characteristics of various combinations of the RK and CD schemes are reported, including dissipation, dispersion, CFL limit, and amount of required artificial damping.

The dispersive characteristic is significantly improved by using the CD4 scheme instead of the conventional CD2 method. Further increasing the order of the CD method, however, results in the little improvement. For both the CD4 and CD6 methods, the smallest wavelength which can be accurately resolved is about four to six grid nodes. On the other hand, the increase of the order of the time stepping scheme enlarges the CFL limit for stable computations. As a result, among all combinations of RKs and CDs considered, we recommend the RK4-CD4 method for simulating unsteady flows.

For practical purposes, the implementation of the nonreflective boundary condition to the present numerical scheme is illustrated. In addition, the initial conditions of the simple wave, plane acoustic wave, and a vortex were also provided. Finally, as illustrated in the numerical examples, for flows of simple harmonic content, e.g., one frequency in case 1, the conventional second-order central difference scheme is adequate provided enough grid nodes are used to resolve the wave mode. On the other hand, for flows of complex harmonic content, the use of the RK4-CD4 and RK4-CD6 methods shows crisp resolution of unsteady flows.

Acknowledgment

The support of the present research by R. M. Stubbs of the NASA Lewis Research Center for the first author, under Contract NAS 3-25266, is greatly appreciated.

References

[1]Colatz, L., *The Numerical Treatment of Differential Equations*, Springer Verlag, New York, 1966, p. 538.

[2]Hirsh, R. S., "Higher Order Accurate Difference Solutions of Fluid Mechanics Problems by a Compact Differencing Technique," *Journal of Computational Physics*, Vol. 19, 1975, pp. 90–109.

[3]Agarwal, R. K., "A Fourth-Order-Accurate Compact Differencing Scheme for Steady Navier–Stokes Equations," AIAA Paper 82-0977, June 1982.

[4]Harten, A., and Tal-Ezer, H., "On a Fourth Order Accurate Implicit Finite Difference Scheme for Hyperbolic Conservation Laws," *Journal of Computational Physics*, Vol. 41, 1981, pp. 329–356.

[5]Philips, R. B., and Rose, M. E., "Compact Finite Difference Schemes for Mixed Initial-Boundary Value Problems," *Journal of Numerical Analysis*, Vol. 19, No. 4, 1982, pp. 698–720.

[6]Ciment, M., and Leventhal, S. H., "A Note on the Operator Compact Implicit Method for the Wave Equation," *Mathematics of Computation*, Vol. 32, No. 141, 1978, pp. 143–147.

[7]Lele, S., "Compact Finite Difference Schemes with Spectral-like Resolution," *Journal of Computational Physics*, Vol. 103, 1992, pp. 16–42.

[8]Carnahan, B., Luther, A. A., and Wilkes, J. O., *Applied Numerical Methods*, John Wiley, New York, 1969, p. 363.

[9]Wray, A. A., "Very Low Storage Time Advancement Schemes," Internal Report, NASA Ames Research Center, Moffett Field, CA, 1986.

[10]Jameson, A., Schmidt, W., and Turkel, E., "Numerical Solutions of the Euler Equations by Finite Volume Methods Using Runge–Kutta Time-Stepping Schemes," AIAA Paper 81-1259, June 1981.

[11]Jameson, A., and Baker, T. J., "Solution of the Euler Equations for Complex Configurations," AIAA Paper 83-1929, July 1983.

[12]Adam, Y., "Highly Accurate Compact Implicit Methods and Boundary Conditions," *Journal of Computational Physics*, Vol. 24, 1977, pp. 10–24.

[13]Vichnevetsky, R., and Bowles, J. B., "Fourier Analysis of Numerical Approximations of Hyperbolic Equations," *Studies in Applied Mathematics*, SIAM, Philadelphia, PA, 1982.

[14]Tsien, H. S., "The Transfer Functions of Rocket Nozzle," *Journal of the American Rocket Society*, Vol. 22, 1952, pp. 139–162.

[15]Williams, F. A., *Combustion Theory*, Benjamin and Cummings, New York, 1985, p. 306.

[16]Anderson, J. D., *Modern Compressible Flow*, McGraw-Hill, New York, 1982, p. 128.

[17]Lighthill, J., *Waves in Fluids*, Cambridge Univ. Press, Cambridge, UK, 1978, p. 142.

[18]Morse, P. M., and Ingard, K. U., *Theoretical Acoustics*, McGraw-Hill, New York, 1968, p. 874.

[19]Liu, N.-S., Davoudzadeh, F., Briley, W. R., and Shamroth, S. J., "Navier–Stokes Simulation of Transonic Blade-Vortex Interactions," *Journal of Fluids Engineering*, Vol. 112, No. 4, 1990, pp. 501–509.

[20]Giles, M. B., "Nonreflecting Boundary Conditions for Euler Equation Calculations," *AIAA Journal*, Vol. 28, No. 12, 1990, pp. 2050–2058.